Journal of Nuclear Materials 407 (2010) 29–33

Contents lists available at ScienceDirect

Journal of Nuclear Materials

journal homepage: www.elsevier.com/locate/jnucmat

SANS investigation of a neutron-irradiated Fe–9 at%Cr alloy

A. Ulbricht [a,*], C. Heintze [a], F. Bergner [a], H. Eckerlebe [b]

[a] Forschungszentrum Dresden-Rossendorf, P.O. Box 510119, 01314 Dresden, Germany
[b] GKSS Forschungszentrum, Max-Planck-Straße, 21502 Geesthacht, Germany

A B S T R A C T

Available experimental results indicate that the addition of Cr to Fe and steels significantly influences the response of Fe–Cr alloys and ferritic/martensitic high-Cr steels to neutron irradiation. A level of 9 at%Cr is of particular interest because this composition is close to the boundary of the Fe–Cr miscibility gap. Furthermore, it corresponds to the composition of several candidate steels for application in nuclear technology. However, experimental evidence has been incomplete so far. The reported study by means of small-angle neutron scattering is devoted to the effect of neutron irradiation at 300 °C up to fluences of 0.6 and 1.5 dpa on the microstructure of an Fe–9 at%Cr alloy. We have observed a pronounced irradiation-induced increase of scattering cross-sections for both magnetic and nuclear scattering. Bimodal size distributions of irradiation-induced defect-solute clusters have been reconstructed. The restrictions on the composition of these clusters have been discussed in terms of the scattering contrast. We have found that vacancy clusters and α′-particles alone cannot explain the full set of experimental findings. The remaining inconsistency can be solved by taking into account a contribution of impurity carbon.

1. Introduction

Ferritic–martensitic chromium steels are candidate materials for future applications in both Gen-IV fission and fusion technology [1,2]. Experimental investigations of Fe–Cr alloys will contribute to the understanding of the effect of chromium on the irradiation behaviour of more complex alloys. Experimental evidence and existing knowledge on the effect of the addition of Cr on the irradiation response has recently been reviewed by Malerba et al. [3]. This response was found to be a highly non-monotonic function of the Cr content.

The effect of Cr on the irradiation-induced microstructure of Fe–Cr alloys was investigated by means of several techniques including TEM, atom probe tomography (APT), positron annihilation spectroscopy (PAS) and small-angle neutron scattering (SANS). It is important to note that there is no single technique capable of exploring all details of the microstructure. TEM studies have been reported for ion- [4,5] and neutron-irradiated [6] binary Fe–Cr alloys. In-situ TEM was applied in order to explain the nature and evolution of irradiation-induced dislocation loops for an Fe–8 at%Cr alloy irradiated with Fe-ions up to 13 dpa [4,5]. The neutron-irradiated Fe–9 at%Cr alloy irradiated up to 0.6 and 1.5 dpa studied in [6] is the same material as the one investigated here. The basic finding is a distribution of irradiation-induced dislocation loops evolving with fluence. In an APT study [7], nm-scale enrichments of Cr often associated with enrichments of C are reported for Fe-ion irradiated Fe–3 at%Cr. The above studies refer to irradiations at a temperature of 300 °C. An investigation of Fe–15.7 at%Cr irradiated at a maximum temperature of 100 °C by means of PAS revealed sub-nm-size vacancy clusters [8]. It seems that SANS investigations of irradiated binary Fe–Cr alloys have not been reported in the literature so far. However, a number of SANS studies was performed for several neutron-irradiated ferritic/martensitic high-Cr steels [9,10]. Depending on neutron fluence and composition these authors found indications for nanovoids, carbides and the Cr-rich α′-phase.

The aims of the present SANS investigation of a neutron-irradiated Fe–9 at%Cr alloy is to reduce the degrees of freedom inherent in the interpretation of the SANS results obtained for complex steels and to complement available [6] and ongoing studies by means of TEM, APT and PAS. Special attention is given to a careful exploitation of the restrictions posed by the SANS results on the composition of the irradiation-induced features.

2. Experiments

2.1. Material and irradiation

The material used in this work was fabricated by SCK·CEN, Mol, Belgium [6]. It was obtained by furnace melting of industrial purity Fe and Cr. After casting, the obtained ingots were cold worked under protective atmosphere to fabricate plates of 9 mm in thickness, treated at 1050 °C for 1 h in high vacuum for austenisation and stabilization and tempered at 730 °C for 4 h followed by air cooling. Composition is summarized in Table 1 [6].

* Corresponding author. Tel.: +49 351 260 3155; fax: +49 351 260 2205.
E-mail address: A.Ulbricht@fzd.de (A. Ulbricht).

0022-3115/$ - see front matter © 2010 Elsevier B.V. All rights reserved.
doi:10.1016/j.jnucmat.2010.07.005

Table 1
Composition of the investigated Fe–9 at%Cr alloy (wt%).

	Mn	Si	P	S	Cr	Ni	C	N	O
Fe–9 at%Cr	0.03	0.09	0.012	0.0007	8.4	0.07	0.02	0.0148	0.066

Neutron irradiation was performed in the framework of the MIRE experiment in the reactor BR2, Mol, Belgium [6]. The irradiation temperature was (300 ± 5) °C. Neutron flux was 9×10^{13} n cm^{-2} s^{-1} ($E > 1$ MeV). The total neutron exposure in terms of displacements per atom (dpa) was 0.6 and 1.5 dpa.

The irradiated material was delivered along with the unirradiated reference as slices $7 \times 7 \times 1$ mm^3.

2.2. Measurements

SANS measurements were performed at the SANS-2 facility of GKSS, Geesthacht, Germany. The samples were placed in a saturation magnetic field of 1.7 T perpendicular to the incident neutron beam direction. A wavelength, λ, of 0.58 nm and three sample-detector distances of 1, 4 and 16 m with corresponding beam collimation lengths were used to cover scattering vectors of magnitude, Q, from 0.1 nm^{-1} to 3 nm^{-1} ($Q = 4\pi \sin\theta/\lambda$, where 2θ is the scattering angle). Scattered neutrons were recorded with an area ^{3}He-detector (50 × 50 cm^2) using 128 × 128 pixels. The measured data were corrected for sample transmission, detector response and background. Macroscopic differential scattering cross-sections, $d\Sigma/d\Omega$, were obtained by calibration against the incoherent scattering of vanadium. The SANS data reduction was carried out using the Sandra [11] software package.

In order to calculate the size distribution of scatterers, a dilute two-phase matrix–inclusion microstructure composed of homogeneous non-magnetic spherical scatterers randomly dispersed in an Fe–9 at%Cr matrix is assumed. For a number of N homogeneous spherical scatterers of radius, R, in the probed volume, V_p, the coherent scattering cross section ($d\Sigma/d\Omega$) can be expressed as:

$$\left(\frac{d\Sigma}{d\Omega}\right)(Q,R) = \frac{N(R)}{V_p}\Delta\eta^2 V^2(R)|F(Q,R)|^2 = c_R(R)\eta^2 V(R)|F(Q,R)|^2 \quad (1)$$

$$|F(Q,R)|^2 = \frac{9(\sin QR - QR\cos QR)^2}{(QR)^6} \quad (2)$$

with the volume, V, of the sphere, the form factor, F, and the volume fraction per size increment, c_R. Magnetic and nuclear scattering are not distinguished in Eq. (1). The scattering contrast, $\Delta\eta^2$, is given by:

$$\Delta\eta_i^2 = \left[(n\bar{b}_i)_C - (n\bar{b}_i)_M\right]^2 \quad (3)$$

where i = mag for magnetic scattering, i = nuc for nuclear scattering, $n = 2/a_0^3$ is the atom number density and a_0 is the lattice parameter of the bcc lattice. Subscripts C and M refer to cluster (scatterer) and matrix, respectively, and $\bar{b}_{mag}$ and $\bar{b}_{nuc}$ denote the average scattering length for magnetic and nuclear scattering, respectively.

The indirect transformation method [12], which is based on a description of the size distribution according to Eqs. (1)–(3), was applied to obtain the size distribution of scatterers without assuming a certain type of distribution.

$$\frac{d\Sigma}{d\Omega}(Q) \rightarrow c_R\Delta\eta^2(R) \quad (4)$$

To this end a number of 40 cubic splines with nodes uniformly distributed in the radius range from 0 to 15 nm were specified by means of a weighted least squares procedure in the present case.

The A-ratio originally defined as ratio of the scattering cross-sections, $d\Sigma/d\Omega$, perpendicular and parallel to the magnetic field direction [13] was calculated according to Eq. (5) from the measured size distributions, c_R, of irradiation-induced scatterers scaled with the (a priori unknown) magnetic and nuclear scattering contrast, $\Delta\eta^2_{mag}$ and $\Delta\eta^2_{nuc}$, respectively. In general, the magnetic and nuclear scattering contrasts are different functions of radius, R. In order to obtain a robust average value of the A-ratio, the size distributions were integrated over R.

$$A = \frac{(d\Sigma/d\Omega)_\perp}{(d\Sigma/d\Omega)_\parallel} = \frac{(d\Sigma/d\Omega)_{mag}}{(d\Sigma/d\Omega)_{nuc}} + 1 = \frac{\int(c_R\Delta\eta^2)_{mag,measured}dR}{\int(c_R\Delta\eta^2)_{nuc,measured}dR} + 1 \quad (5)$$

After completion of the SANS experiments, Vickers hardness, HV10, was measured according to standard DIN 50133 using the same samples. A number of 10 hardness tests were performed for each condition.

3. Results

The separated magnetic and nuclear contributions to the total scattering cross section are presented in Fig. 1 for both irradiation conditions as well as the unirradiated control. There is a pronounced irradiation-induced increase of scattering cross-sections in the Q-range from 0.2 to 3 nm^{-1}. The difference between the two irradiation conditions is small but significant. Straight lines corresponding to a Q^{-4}-dependence and estimations of the incoherent scattering are indicated for comparison.

Incoherent scattering for the unirradiated condition was determined from a Porod plot giving more exact results than direct estimation from Fig. 1. We have obtained a value of incoherent nuclear scattering, $(d\Sigma/d\Omega)_{inc} = (0.0076 \pm 0.0003)$ cm^{-1} sr^{-1}. The theoretical value calculated from the isotopic composition of Fe and Cr and from the Fe–Cr mixing term [14] is 0.00593 cm^{-1} sr^{-1}. It does

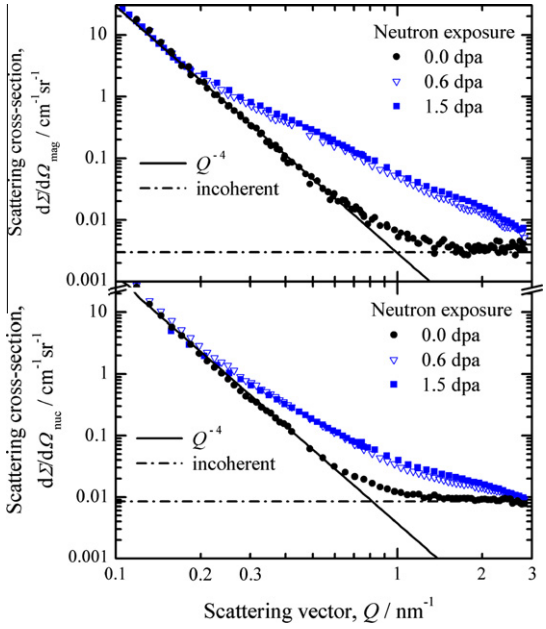

Fig. 1. Measured magnetic and nuclear scattering cross-sections as a function of the scattering vector, Q.

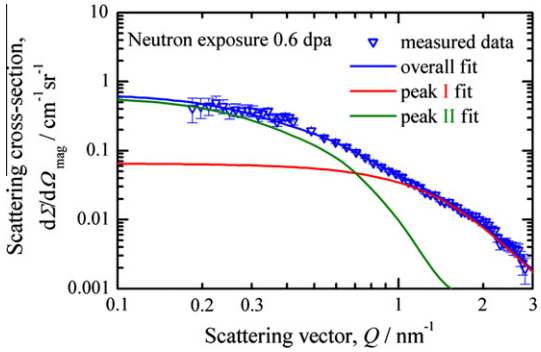

Fig. 2. Magnetic difference scattering curve for Fe–9 at%Cr irradiated up to 0.6 dpa.

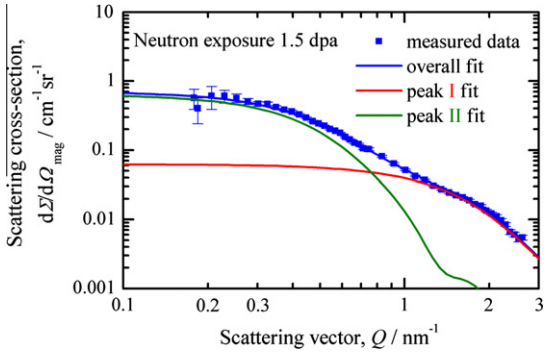

Fig. 3. Magnetic difference scattering curve for Fe–9 at%Cr irradiated up to 1.5 dpa.

explain the major part of the measured value. The remainder is assumed to be due to impurities and lattice defects.

The size distribution of scatterers was calculated by means of fitting the magnetic difference scattering curves (Figs. 2 and 3). Our standard procedure according to [12] does not assume a certain type of size distribution. In the first iteration we have observed that the size distributions are essentially bimodal. Therefore, the following approach was chosen: The first component of the bimodal size distribution (Fig. 4) was reconstructed by fitting the difference scattering curves at high values of Q, $1\ \mathrm{nm}^{-1} < Q < 3\ \mathrm{nm}^{-1}$ (Figs. 2 and 3). The result was subtracted from the difference scattering curve and fitted in order to obtain the second component (Fig. 4). It turned out that the sum of the two scattering curves calculated individually from the reconstructed components of the bimodal size distribution fits the measured scattering cross section in the whole Q-range very well (Figs. 2 and 3).

In the calculations, we have assumed the scatterers to be magnetic holes in a ferromagnetic Fe–9 at%Cr matrix. If the scatterers

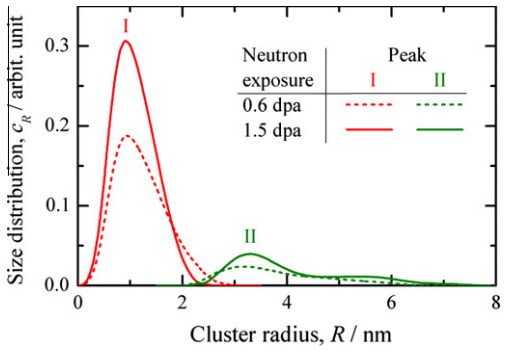

Fig. 4. Reconstructed bimodal size distributions for both irradiation conditions.

Table 2
Summary of the results for the irradiation-induced changes of microstructure and Vickers hardness.

Neutron exposure		0.6 dpa	1.5 dpa
Volume fraction, c (%)	$R < 2.4$ nm	0.25 ± 0.005	0.35 ± 0.005
	2.4 nm < R < 7 nm	0.06 ± 0.01	0.08 ± 0.01
A-ratio	$R < 2.4$ nm	2.85 ± 0.1	2.65 ± 0.1
	2.4 nm < R < 7 nm	2.4–3	2.4–3
Hardness change, ΔHV10		74 ± 10	75 ± 10

do not bear a magnetic moment, the calculated size distributions given in Fig. 4 are correct in units of vol%. Otherwise, the calculated size distributions will be correct in relative units and serve as lower bounds for the possible real size distributions.

We have applied the same procedure to the nuclear scattering cross section thus confirming the two components. Finally, the total volume fraction and the average A-ratio have been calculated according to Eqs. (4) and (5) separately for both components, $R < 2.4$ nm (component I) and 2.4 nm < R < 7 nm (component II). The results are summarized in Table 2 along with the measured irradiation-induced increase of Vickers hardness, ΔHV10. It is important to note that the error of the volume fraction for the second component is about twice the error for the first component, because, according to our analysis, the error for component I is additionally propagated to component II. A similar, but more qualitative reasoning is applicable to the error of the A-ratio. The error of the hardness change was obtained from the standard deviation for a number of 10 hardness tests for each condition. The volume fractions given in Table 2 in units of vol% are those obtained on the assumption of non-magnetic scatterers as discussed above.

4. Discussion

4.1. Size distribution

The two components of the size distribution identified in Section 3 for neutron exposures of both 0.6 and 1.5 dpa slightly overlap each other. Nevertheless, it seems to be reasonable to assign components I and II approximately to the size ranges, $R < 2.4$ nm and 2.4 nm < R < 7 nm, respectively. Components I and II are treated separately below as if the corresponding objects belonged to different populations (denoted I and II, respectively).

Restricting to the viewpoint of the size of irradiation-induced features for the moment, it is reasonable to suppose that population II is related to the dislocation loops investigated by means of TEM in the same irradiated Fe–9 at%Cr alloy. In fact, the mean diameters of these loops were estimated to be 7 nm and 13 nm for the 0.6 and 1.5 dpa irradiations, respectively [6]. This is in the size range of population II. The size range derived from a more detailed TEM study [4,5] on the nature and evolution of loops with fluence in Fe–8 at%Cr is also in agreement with the size range observed for population II. However, it is important to mention that the theoretical scattering cross section arising from pure (undecorated) dislocation loops [15] is too small to explain the measured volume fractions for population II [16,17]. This is due to the difference of both the form factor and the contrast between planar loops and spherical precipitates.

Population I is supposed to consist of tiny volumetric features at sizes below the detection limit of the reported TEM studies. SANS experiments performed for Cr-steels of similar Cr-contents report the possible presence of vacancy clusters, α′-particles [9] and C–Cr aggregates [18] in the size range corresponding to population I, but are not fully conclusive. Cr-enriched clusters associated with C were also reported for an Fe–3%Cr alloy in an APT study [7].

The nature of populations I and II will be reconsidered in Sections 4.3 and 4.4.

4.2. Volume fraction and hardness

The volume fraction corresponding to population I increases significantly with increasing neutron fluence. The increase is slower than linear in the sense that the exponent of a power–law relation between volume fraction and fluence would be less than 1. The volume fractions corresponding to population II are about four times smaller and increase with fluence at about the same proportion as population I, but the increase is less significant because of larger relative errors.

The hardness values obtained for the two levels of fluence agree with one another within the range of errors. The given errors are obtained from the standard deviations from a number of 10 hardness tests for the irradiated and unirradiated conditions. The relatively high values of the standard deviation indicate that there are spatial variations of hardness. Typically, a strong correlation between Vickers hardness increase and square root of volume fraction is observed [19]. Taking into account errors the present results do not exclude this possibility. Another interpretation for the absence of an increase of ΔHV10 with fluence could be related to the possibility that an increase of volume fraction with fluence is compensated by a simultaneous reduction of the obstacle strength posed by the scatterers to dislocation glide.

4.3. A-ratio for binary Fe–Cr

In order to exploit the information encoded in the measured *A*-ratio, the range of *A*-ratios accessible in the binary system Fe–Cr is considered first. It is assumed that the scatterers consist of Cr-atoms (magnetic scattering length, $b_{\mathrm{magCr}} = 0$), Fe-atoms ($b_{\mathrm{magFe}} = 6$ fm) and vacancies in a matrix consisting of Fe and 9 at%Cr and that linear super-position of magnetic moments is applicable. Magnetic scattering lengths modified due to the interaction of Fe and Cr are discussed later. The *A*-ratio can be expressed as:

$$A = 1 + \frac{\Delta\eta^2_{\mathrm{mag}}}{\Delta\eta^2_{\mathrm{nuc}}} = 1 + \left(\frac{b_{\mathrm{magFe}}}{b_{\mathrm{nucFe}}}\right)^2 \left(\frac{1-\beta_{\mathrm{magCr}}+\delta}{1-\beta_{\mathrm{nucCr}}+\delta}\right)^2 \tag{6}$$

where

$$\beta_{\mathrm{magCr}} = \frac{b_{\mathrm{magCr}}}{b_{\mathrm{magFe}}} = 0, \beta_{\mathrm{nucCr}} = \frac{b_{\mathrm{nucCr}}}{b_{\mathrm{nucFe}}} = 0.384, \text{and } \delta = \frac{a_{\mathrm{VC}}}{a_{\mathrm{CrC}} - a_{\mathrm{CrM}}} \tag{7}$$

The quantities a_{Cr}, a_{Fe} and a_{V} denote the fractions of lattice sites occupied by Cr-atoms, Fe-atoms, and vacancies, respectively. $a_{\mathrm{CrC}} + a_{\mathrm{FeC}} + a_{\mathrm{VC}} = 1$ for clusters (C), and $a_{\mathrm{CrM}} = 0.09$, $a_{\mathrm{FeM}} = 0.91$, $a_{\mathrm{VM}} = 0$ for the matrix (M).

The *A*-ratio is plotted in Fig. 5 as a function of the composition parameter, δ, according to Eq. (7). For scatterers free of vacancies ($\delta = 0$), the *A*-ratio assumes a value of 2.05 independently of the Fe-fraction. For vacancy-containing scatterers enriched with Cr ($\delta > 0$) the *A*-ratio assumes values, $1.4 < A < 2.05$. For Cr-depleted vacancy-containing scatterers, the *A*-ratio may assume any value, $1 \leqslant A < \infty$, depending on the value of δ. The special value $A = 1$ appears, if $\delta = -1$, i.e. if vacancies replace Cr-atoms only.

In the case that there are magnetic interactions between Fe-atoms and Cr-atoms, linear super-position is no longer applicable. In [20,21] it is reported that the deviations can be expressed as $\bar{b}_{\mathrm{mag}} = b_{\mathrm{magFe}} - \alpha_{\mathrm{mag}} a_{\mathrm{Cr}}$ with $\alpha_{\mathrm{mag}} = 6.32$ (instead of $\alpha_{\mathrm{mag}} = 6$ for linear super-position). Accordingly, the value of 2.05 obtained above has to be replaced by a slightly corrected value of 2.18 independently of the Cr-fraction.

The analysis implies that the measured range of *A*-ratios, $2.4 < A < 3$, is only possible, if the dominant type of scatterers is Cr-depleted relative to the matrix. Furthermore, the measured *A*-ratio poses a restriction on the scattering contrast, $\Delta\eta^2_{\mathrm{mag}}$, normalized in Eq. (8) with the contrast for a magnetic hole, $\Delta\eta^2_{\mathrm{ref}}$. In fact,

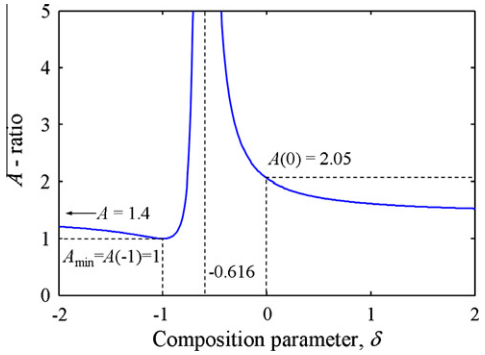

Fig. 5. *A*-ratio calculated for scatterers composed of Cr-atoms, Fe-atoms and vacancies confined to bcc lattice sites as a function of the composition parameter, δ, according to Eq. (7).

from $A \geqslant 2.65$ for the 1.5 dpa irradiation one obtains $\delta \leqslant -0.25$ and, therefore,

$$\frac{\Delta\eta^2_{\mathrm{mag}}}{\Delta\eta^2_{\mathrm{ref}}} = \frac{\left(b_{\mathrm{magFe}}a_{\mathrm{FeC}} - b_{\mathrm{magFe}}a_{\mathrm{FeM}}\right)^2}{\left(0 - b_{\mathrm{magFe}}a_{\mathrm{FeM}}\right)^2} = (1+\delta)^2(a_{\mathrm{CrC}} - a_{\mathrm{CrM}})^2 \leq 0.75^2 \cdot 0.09^2 = 0.0046 \tag{8}$$

Another restriction on the contrast is posed by the integrated intensity, *I*, which is a well-known invariant value of scattering theory [14]:

$$I = \int_0^\infty \frac{\mathrm{d}\Sigma}{\mathrm{d}\Omega}(Q) 4\pi Q^2 \,\mathrm{d}Q = (2\pi)^3 c(1-c)\Delta\eta^2 \leq 2\pi^3\Delta\eta^2 \tag{9}$$

A value, $I = 2.59\ \mathrm{cm}^{-1}\ \mathrm{nm}^{-3}$, was obtained from the experimental results for the 1.5 dpa irradiation. Using $\Delta\eta^2_{\mathrm{ref}} = 2.128\ \mathrm{cm}^{-1}\ \mathrm{nm}^{-3}$, it is strictly shown that the restrictions posed by Eqs. (8) and (9) are in conflict. The same applies to the 0.6 dpa irradiation. As a consequence of this section, any type of clusters composed of Cr-atoms, Fe-atoms and vacancies confined to bcc lattice sites in an Fe–9 at%Cr matrix is inconsistent with the set of experimental results. In particular, pure vacancy cluster and the α′-phase are included in this family of clusters. In other words, there must exist another type of features contributing to the irradiation-induced scattering.

4.4. Effect of impurity carbon

The impurity carbon concentration according to the chemical analysis corresponds to about 0.1 at%. It is well known that Cr and C form carbides of considerable stability. Atom probe investigation of an Fe–Cr alloy revealed irradiation-induced nm-scale enrichments of carbon associated with enrichments of Cr [7]. Furthermore, SANS investigations of unirradiated ferritic–martenistic Cr-steels also revealed nm-scale coaggregations of Cr- and C-atoms depending on heat treatment [18]. It is therefore reasonable to include Cr–C aggregates as additional candidates for the observed scattering into the present analysis.

As the structure of such Cr–C aggregates is not known with certainty and probably not well defined, exact theoretical values of the *A*-ratio cannot be derived. However, the theoretical *A*-ratio was calculated from the structure data [22,23] of two types of Cr-carbides (Table 3). Other types of carbides, in particular iron carbides, are characterized by still higher values of *A*. The smallest *A*-ratio among the known types of Fe- and Cr-carbides is observed for $Cr_{23}C_6$. It is also important to mention that the total amount of carbon in the present alloy is sufficient to realize the measured volume fractions.

Comparison of the experimental range of *A*-ratios for both irradiation conditions and for both components of the size distribu-

Table 3
A-ratio calculated for selected types of scatterers in an Fe–9 at%Cr matrix.

Type of scatterer	Theoretical *A*-ratio
Nanovoids	1.37
α'-phase	2.05–2.18
$Cr_{23}C_6$	2.93
Cr_7C_3	3.70

tions, $2.4 \leqslant A \leqslant 3$, with the calculated values according to Table 3 and Section 4.3 indicate that:

(1) nanovoids, α'-particles and any type of mixed coherent Cr–Fe-vacancy clusters alone are not consistent with the SANS results,
(2) Cr-rich carbides and mixed Fe–Cr carbides alone are also not consistent with the SANS results,
(3) a mixture of features according to points (1) and (2) can explain the full set of experimental findings,
(4) the observed irradiation-induced features can also be a transition form between C-free Cr-rich precipitates (e.g. α') and Cr-rich carbides.

The latter interpretation is in agreement with nm-scale Cr–C aggregates observed in unirradiated Cr-steels [18].

The interpretation according to points (3) and (4) applies equally well to populations I and II. The difference may be that population I nucleates homogeneously in the volume, whereas population II is associated with dislocation loops which are attractive for both Cr and C.

5. Conclusion

SANS experiments performed for an industrial purity Fe–9 at%Cr alloy neutron-irradiated up to 0.6 and 1.5 dpa indicate that

- for both irradiation conditions there are two populations of irradiation-induced features with size (radius) in the ranges, $R < 2.4$ nm and $2.4\ \text{nm} < R < 7$ nm, respectively,
- the total volume fraction of irradiation-induced features slightly increases with neutron fluence,
- the measured value of the *A*-ratio is higher than those expected for nanovoids and α'-particles, but smaller than those expected for well-developed Cr-carbides, that means either a mixture of both or a transition form could explain the experimental results.

Vickers hardness tests indicate an irradiation-induced hardness increase but do not reveal a significant difference between both irradiation conditions.

Acknowledgment

This research has been partly supported by the European Commission within the collaborative project GETMAT under Grant Agreement No. 212175. The authors would like to thank M. Matijasevic and A. Almazouzi (SCK·CEN) for providing the material along with basic documentation.

References

[1] R.L. Klueh, A.T. Nelson, J. Nucl. Mater. 371 (2007) 37.
[2] I. Cook, Nat. Mater. 5 (2006) 77.
[3] L. Malerba, A. Caro, J. Wallenius, J. Nucl. Mater. 382 (2008) 112.
[4] Z. Yao, M. Hernandez-Mayoral, M.L. Jenkins, M.A. Kirk, Philos. Mag. 88 (2008) 2851.
[5] M. Hernandez-Mayoral, Z. Yao, M.L. Jenkins, M.A. Kirk, Philos. Mag. 88 (2008) 2881.
[6] M. Matijasevic, A. Almazouzi, J. Nucl. Mater. 377 (2008) 147.
[7] E.A. Marquis, A. Cerezo, Atom probe tomography observations of irradiation-induced clustering in Fe–Cr alloys, in: Poster presented at the 13th Int. Conf. on Fusion Reactor Materials, Nice, December 2008.
[8] V.L. Arbuzov, A.P. Druzhkov, A.L. Nikolaev, S.M. Klotsman, Radiat. Effects Defects Solids 124 (1992) 409.
[9] M.H. Mathon, Y. de Carlan, G. Geoffroy, X. Averty, A. Alamo, C.H. de Novion, J. Nucl. Mater. 312 (2003) 236.
[10] R. Coppola, R. Lindau, R.P. May, A. Möslang, M. Valli, J. Nucl. Mater. 386–388 (2009) 195.
[11] See <http://www.genf.gkss.de>.
[12] O. Glatter, J. Appl. Cryst. 13 (1980) 7.
[13] G. Solt, F. Frisius, W.B. Waeber, P. Tipping, in: A.S. Kumar, D.S. Gelles, R.K. Nanstadt, E.A. Little, (Eds.), Effects of Radiation on Materials: 16th Int. Symp. ASTM STP 1175, ASTM, Philadelphia, 1993, p. 444.
[14] P. Lindner, T. Zemb, Neutron, X-rays and Light: Scattering Methods Applied to Soft Condensed Matter, Elsevier, Amsterdam, 2002.
[15] A. Seeger, M. Rühle, Ann. Phys. 11 (1963) 216–229.
[16] J. Henry, M.-H. Mathon, P. Jung, J. Nucl. Mater. 318 (2003) 249.
[17] F. Bergner, A. Ulbricht, M. Hernandez-Mayoral, P.K. Pranzas, J. Nucl. Mater. 374 (2008) 334.
[18] R. Coppola, R. Kampmann, M. Magnani, P. Staron, Acta Mater. 46 (1998) 5447.
[19] A. Ulbricht, J. Böhmert, H.-W. Viehrig, J. ASTM Int. 2 (2005) JAI12385.
[20] A.T. Aldred, B.D. Rainford, J.S. Kouvel, T.J. Hicks, Phys. Rev. B 14 (1976) 228–234.
[21] W. Pepperhoff, M. Acet, Constitution and Magnetism of Iron and its Alloys, Springer-Verlag, Berlin, Heidelberg, 2001.
[22] D.J. Dyson, K.W. Andrews, J. Iron Steel Inst. (1969) 208.
[23] M. Gao, R.P. Wei, Scripta Metall. Mater. 30 (1994) 1009.